

Measuring Superconducting
Stiffness and Coherence of
Magnetic Materials with
Zero-Applied Field, and
Application to FeSeTe

Amotz Peri

Measuring Superconducting Stiffness and Coherence of Magnetic Materials with Zero-Applied Field, and Application to FeSeTe

Research Thesis

Submitted in partial fulfillment of the requirements
for the degree of Master of Science in Physics

Amotz Peri

Submitted to the Senate
of the Technion — Israel Institute of Technology
Elul 5782 Haifa August 2022

This research was carried out under the supervision of Prof. Amit Keren, in the Faculty of Physics.

The Technion's funding of this research is hereby acknowledged.

Contents

List of Figures

Abstract	1
Abbreviations and Notations	3
1 Introduction	5
1.1 Superconductivity	5
1.2 FeSeTe	6
1.3 London equation	7
2 Stiffnessometer Principles	9
2.1 Experimental setup	9
2.2 SQUID magnetometer	11
3 Measurements	13
3.1 Stiffness	13
3.2 Susceptibility	16
3.3 Hysteresis loop	16
3.4 Critical magnetic fields	17
4 Analysis Model	19
4.1 Stiffness	19
4.2 Coherence length	21
5 Data Analysis	23
6 Discussion and Conclusion	25
6.1 Comparison with theory	25
6.2 Conclusion	27
A Mathematical Description	29
A.1 London equation derivation	29
A.2 Coherence length – approximate theory	30

A.3 Free iron ions in the sample	32
B Gradiometer	33
C Temperature calibration	35
D Knee Investigation	39
D.1 Applied field influence	39
D.2 Rings comparison	40
D.3 Nematic order	41
D.4 Two critical temperatures?	42
Hebrew Abstract	i

List of Figures

1.1	FeSeTe crystal structure	6
2.1	Experimental structure	10
2.2	Stiffnessometer DC scan	12
3.1	Superconducting magnetic moment vs. current in the excitation-coil; Moment vs. temperature; and critical current vs. temperature	15
3.2	Magnetic hysteresis; and critical fields measurements	18
5.1	Penetration depth and coherence length	24
A.1	Illustration of the evolution of the current density in a superconducting cylinder	31
C.1	Temperature calibration	36
C.2	Critical currents before and after the calibration; and temperature cor- rections	37
C.3	Temperature calibration errors	37
C.4	Leaking field from the excitation coil	38
D.1	Knee investigation	40
D.2	Rings comparison – moment vs. temperature	41
D.3	Phase diagram of $\text{FeSe}_x\text{Te}_{1-x}$. Nematic and superconducting transition temperatures vs. Te composition	42
D.4	Surface superconductivity illustration	42

Abstract

Superconductivity in the Iron-chalcogenide FeSeTe was discovered in the last two decades. Its critical temperature rises up to 15 K at ambient pressure for optimal doping.

Superconducting stiffness ρ_s and coherence length ξ are usually determined from the penetration depth λ of a magnetic field and the upper critical field H_{c2} of a superconductor (SC), respectively. However, in magnetic SCs, e.g., part of the iron-based, this could lead to erroneous results since the field couples to the magnetic moments. To overcome this problem in FeSeTe, we measure both quantities with the Stiffnessometer technique. In this technique, one applies a current in a thin and long excitation coil. This current creates a rotor-free vector potential \mathbf{A} to a superconducting ring held in its center. According to London's equation $\mathbf{j} = -\rho_s \mathbf{A}$, current density emerges \mathbf{j} which is measured via the ring's magnetic moment \mathbf{M} using a superconducting quantum interference device (SQUID). ρ_s and ξ are determined from London's equation and its range of validity. This method does not suffer from demagnetization factors complications or the presence of vortices and is particularly accurate close to the critical temperature T_c . This work contains a comparison between measurements by several techniques, surprising results such as unexpected and intended heating of the superconductor and the appearance of a peculiar knee. We find longer ρ_s and ξ than previously thought, and a phase transition which agree better with expectations based on the Ginzburg–Landau theory.

Abbreviations and Notations

ARPES	: Angle-Resolved Photoemission Spectroscopy
EC (ec)	: Excitation Coil
FeSeTe	: Ferrum, Seleniom and Tellurium
GL	: Ginzburg-Landau
IBS/FeBS	: Iron/Ferrum-Based Superconductor
μ SR	: Muon Spin Relaxation
PDE	: Partial Differential Equation
PL (pl)	: Pickup-Loop
RF	: Radio Frequency
SC (sc)	: Superconductor
SQUID	: Superconducting Quantum Interference Device
STM	: Scanning Tunneling Microscope
VSM	: Vibrat Sample Magnetometer
ZFC	: Zero Field Cooling
ZGFC	: Zero Gauge-Field Cooling

A	:	Vector Potential
B	:	Magnetic Induction
D	:	Demagnetization Factor
e^*	:	Charge Carrier
g	:	Calibration Constant
H	:	External Magnetic Field
H_{c1}	:	First Superconducting Critical Field
H_{c2}	:	Second Superconducting Critical Field
I	:	Current
I_c	:	Critical Current
j	:	Superconducting Density Current
J	:	Normalized Magnetic Flux
M	:	Magnetic Moment
m^*	:	Charge Carrier Mass
m_ρ	:	Critical Exponent of the Stiffness
m_ξ	:	Critical Exponent of the One Over ξ
n	:	Winding Density of the Excitation Coil
n_s^*	:	Charge Carrier Density
T	:	Temperature
T_c	:	Superconducting Critical Temperature
T_s	:	Nematic Transition Temperature
V	:	Volume
χ	:	Measured Magnetic Susceptibility
χ_0	:	Specific Magnetic Susceptibility
μ_0	:	Vacuum Permeability
λ	:	Penetration Depth
ϕ	:	Phase of the Complex Order Parameter
Φ	:	Magnetic Flux
Φ_0	:	Flux Quanta
ψ	:	Complex Order Parameter Magnitude
Ψ	:	Complex Order Parameter
ρ_s	:	Superconducting Stiffness
$\hat{\varphi}$:	Azimuthal Direction
ξ	:	Ginzburg-Landau Coherence Length

Chapter 1

Introduction

1.1 Superconductivity

Superconductivity is a particular phase characterized by many unique phenomena such as zero resistance and perfect diamagnetism (Meissner Effect). Classical superconductor (SC) can be explained by the BCS theory (named after John Bardeen, Leon Cooper, and John Robert Schrieffer), which considers attractive interaction between electrons through electron-phonon occupying. It is common to think of the charge carriers of a SC as pairs of electrons called Cooper-Pairs, rather than individual electrons. The critical temperature T_c refers to the transition temperature between the superconducting and the normal phases.

The coherence length ξ is the shortest length scale over which the phase of the complex order parameter can vary. It is also common to think of ξ as the size of a flux vortex radius. When applying a magnetic field, the SC will reject it by creating supercurrents that screen the external magnetic field. If we increase the external field, the supercurrents will also increase. But although the field is expelled from the bulk, it penetrates along the edges with an exponential decay with some characteristic length known as the penetration depth λ .

Superconducting materials can be divided into two types, depending on the ratio of ξ and λ . Type-I SC have $\lambda < \xi/\sqrt{2}$ and type-II SC have $\lambda > \xi/\sqrt{2}$. A type-I SC will hold the magnetic field outside until it reaches its critical field H_c . Above H_c , the material gives up and transforms back to the normal state letting all the magnetic flux going through it. Type-II SC will stay field-free up to some critical field H_{c1} . Beyond this value, some magnetic flux manages to penetrate as vortices. The core of the vortex will be in the normal state phase, but outside the vortex, the material will remain superconducting. When we increase the field, more and more vortices will penetrate until they cover the entire material in the second critical field H_{c2} .

1.2 FeSeTe

The highest T_c measured in bulk Iron-based superconductors (IBSs), in ambient pressure, is 56 K [1], higher than some cuprates. Consequently, they have been at the forefront of research in the solid-state community. Out of all IBSs, the crystalline structure of the FeSe is the simplest see Fig. 1.1. By partially replacing Se with Te atoms, the critical temperature increases up to 15 K, obtained at $x = 0.45$ $y \simeq 0$ in the formula $\text{Fe}_{1+y}\text{Se}_x\text{Te}_{1-x}$. As summarized in Ref. [2], the material also possesses surprising properties such as highly anisotropic electronic properties (nematic effects) and evidence for topologically non-trivial bands and superconductivity. In light of these properties, it is important to characterize FeSeTe as accurately as possible.

Bulk DC superconducting properties, such as the stiffness ρ_s , were measured by transverse field muon spin rotation (μSR) [3, 4]. AC measurements were done by RF tunnel diode [5, 6] and cavity perturbation [7] techniques. Coherence length measurements of FeSeTe with $x = 0.45$ were done by vortex size ξ using a scanning tunneling microscope (STM) [8], angle-resolved photoemission spectroscopy (ARPES) [9], and resistivity measurements [10]. However, due to the presence of Fe in the structure and residual magnetism, these measurements might not provide a clear in-sight into the superconducting properties since the applied field interacts with a magnetic moment in addition to the superconducting currents. In this work, we measure DC superconducting properties in a zero-applied field to avoid contamination from magnetism.

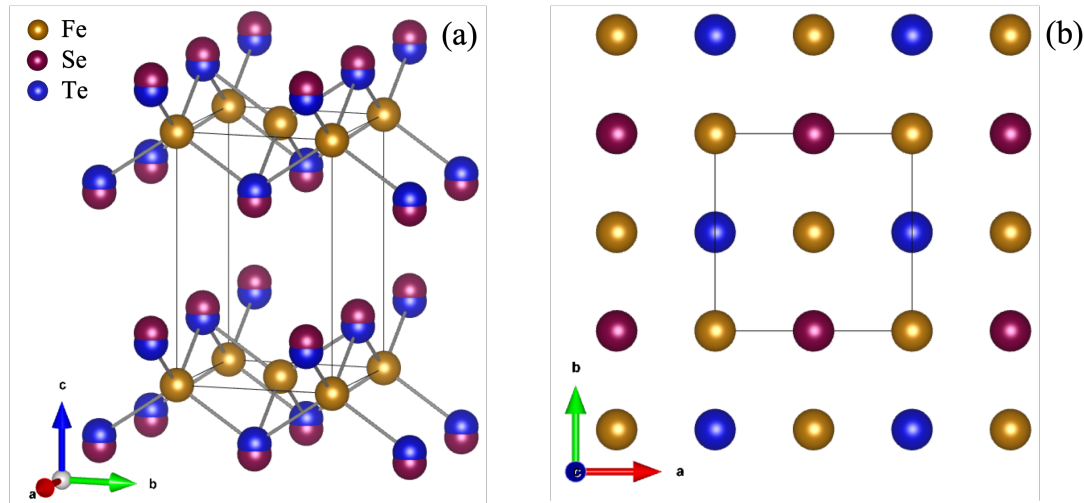


Figure 1.1: Illustration of the crystal structure of $\text{FeSe}_{0.5}\text{Te}_{0.5}$. The data was taken from Ref. [11].

The crystal structure of $\text{FeSe}_x\text{Te}_{1-x}$, with the $P4/nmm$ symmetry, is illustrated from two different angles in Fig. 1.1. In this symmetry, the Se and Te atoms share the same site. The gold-colored balls are iron atoms, and the maroon/blue are Se/Te ones. The iron atoms form a square lattice, each is connected to four Se/Te atoms. Its unit cell, marked in a black box frame, is tetragonal (lattice parameters: $a = b = 3.792 \text{ \AA}$,

$c = 3.792 \text{ \AA}$), and contains two iron atoms and two Se/Te atoms. The Fermi surface of the $\text{FeSe}_{0.5}\text{Te}_{0.5}$ consists of two small hole pockets around γ and two electron pockets around the M -point of the Brillouin zone [2].

1.3 London equation

The superconducting stiffness ρ_s is defined via the gauge-invariant relation between the current density \mathbf{j} , the total vector potential \mathbf{A}_{tot} from all sources, and the complex order parameter $\Psi(\mathbf{r}) = \psi(\mathbf{r})e^{i\phi(\mathbf{r})}$ with $\psi(\mathbf{r}) > 0$, according to

$$\mathbf{j} = -\rho_s \left(\mathbf{A}_{\text{tot}} - \frac{\Phi_0}{2\pi} \nabla \phi \right), \quad (1.1)$$

where $\Phi_0 = 2\pi\hbar/e^*$ is the superconducting flux quanta,

$$\rho_s = \frac{\psi^2 e^{*2}}{m^*}, \quad (1.2)$$

is the stiffness, e^* and m^* are the carrier's charge and mass, respectively. An extended mathematical description of the gauge-invariant London equation appears in Appx. A.1. This equation contains two degrees of freedom. One is the gauge field, and the other is the multiple branches of the order parameter phase ϕ . Both are determined such that the free energy is minimal. Therefore, when cooling the SC with $\mathbf{A}_{\text{tot}} = 0$ in the London gauge, $\nabla\phi = 0$ and, according to the second Josephson relation, it can only change by dissipating energy. Thus, Eq. 1.1 becomes the London equation

$$\mathbf{j} = -\rho_s \mathbf{A}_{\text{tot}}. \quad (1.3)$$

This relation holds as long $\nabla\phi$ does not change. The stiffness, in turn, is related to the penetration depth via

$$\rho_s = \frac{1}{\mu_0 \lambda^2}. \quad (1.4)$$

However, every superconductor has a critical current density j_c determined by the penetration depth λ and coherence length ξ . When \mathbf{A}_{tot} exceeds a certain value, it is worthwhile for the SC to change $\nabla\phi$ so as to keep j below j_c everywhere in the SC while dissipating energy in the process. When this happens, the relation between \mathbf{j} and \mathbf{A}_{tot} is no longer linear, and the system's rigidity breaks. We used these properties to measure both ρ_s and ξ in FeSeTe.

Chapter 2

Stiffnessometer Principles

In this chapter, we will explain our technique's operation principles. We called it Stiffnessometer because it is used to measure superconducting stiffness. In order to investigate the SC, we shape it into a ring and place it in the center of a long excitation coil (EC) (ideally, it is infinitely long). When we apply current I through the excitation coil, a magnetic field is generated only inside the coil. Nonetheless, there is a rotor-free vector potential outside the coil $\mathbf{A} = \frac{\mu_0 n I r_{ec}^2}{r} \hat{\phi}$, where n is the winding density and r is the distance from the coil's symmetry axis. If we cool the sample below T_c without any magnetic field or current in the excitation coil, the vector potential is zero $\mathbf{A} = 0$. This cooling process is called Zero Gauge-Field Cooling (ZGFC). When cooling in this way, there is nothing in the system that can accelerate currents in the ring. So for Eq. 1.1 to hold, $\nabla\phi = 0$ is required, and the London equation (Eq. 1.3) is obtained. However, when the sample is superconducting, a change in ϕ has an energy cost. Consequently, the linear relation $\mathbf{j} = -\rho_s \mathbf{A}$ remains, and a change of the vector potential \mathbf{A} induces changes in the superconducting current density \mathbf{j} in the ring. This current goes around the ring in loops and creates a magnetic moment M that can be detected by a pickup-loop connected to a superconducting quantum interference device (SQUID). Since \mathbf{A} is proportional to the current in the excitation coil I_{ec} , and \mathbf{j} is proportional to the sample's magnetic moment M we get a linear relation between the applied current and the measured signal. When this linearity breaks, we know something has changed in the system, and we are out of the linear regime.

2.1 Experimental setup

The system is assembled from a ring-shaped SC, cut out of a single crystal with a femtosecond laser, as presented in Fig. 2.1(a). A long excitation coil pierces the ring. Both appear in panel (b). The excitation coil, ring, and a second-order gradiometer are connected to a SQUID system and surrounded by a main coil used to zero the field to less than $0.1 \mu\text{T}$ on the ring, and for field-dependent measurement, as in panel (c). Details of the dimensions of the different parts are given in the figure caption. The

current flows in the excitation coil generate a vector potential \mathbf{A}_{ec} on the ring without a magnetic field H . This vector potential is responsible for persistent rotational current in the superconducting ring. This rotational current produces its own vector potential \mathbf{A}_{sc} and a magnetic moment. The vector potential in Eq. 1.1 is $\mathbf{A}_{\text{tot}} = \mathbf{A}_{\text{ec}} + \mathbf{A}_{\text{sc}}$. The magnetic moment is detected by moving the ring with the excitation coil rigidly relative to the gradiometer. More information about how the gradiometer works appears in Appx. B. The gradiometer and SQUID are part of QD-MPMS3 magnetometer. We used the vibrating sample magnetometer (VSM) mode to measure the ring's magnetic moment M .

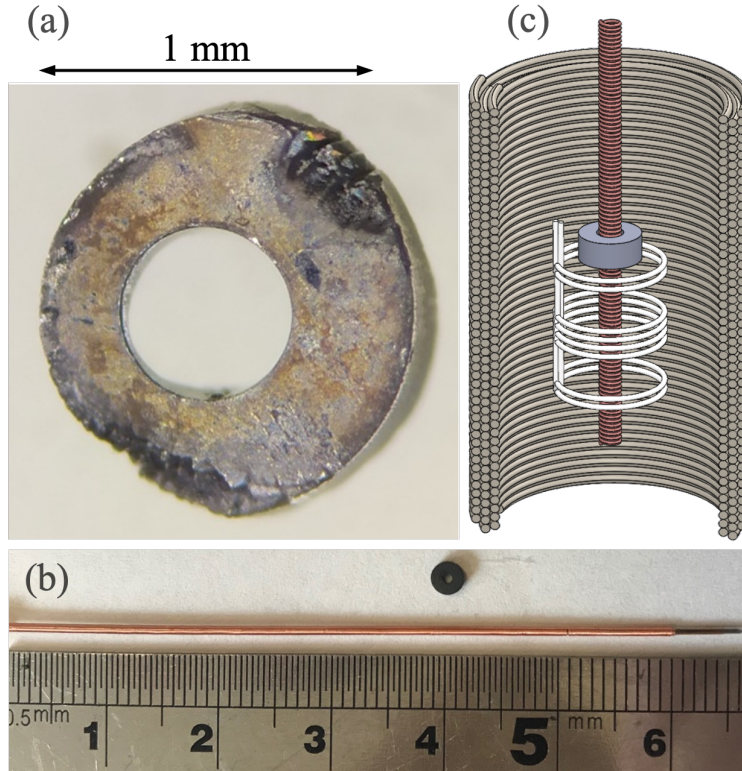


Figure 2.1: Experimental structure. (a) A microscopic image of the $\text{FeSe}_{0.5}\text{Te}_{0.5}$ ring. The sample is not uniform. The minimal height, inner and minimal outer radii are $h = 0.10$ mm, $r_{\text{in}} = 0.26$ mm, and $r_{\text{out}} = 0.50$ mm respectively. A discussion of asymmetry in the ring's outer radius appears in Sec. 4.1. (b) A copper excitation coil with a superconducting ring beside it. The coil has a length of 60 mm, an outer diameter of 0.25 mm, and 9300 turns in two layers. This coil is connected to an external current source. (c) The ring and excitation coil assembly is moving rigidly relative to a gradiometer, connected to a SQUID system, and surrounded by a main coil for field zeroing or field-dependent measurement. The SQUID, gradiometer, and main coil are part of a QD-MPMS3 system.

In principle, \mathbf{A}_{ec} does not change as the coil vibrates (no excitation coil flux variation), and the pickup-loop signal is only due to \mathbf{A}_{sc} (in practice, the signal of the excitation coil is reduced from the measurements as background, as depicted in Sec. 3.1).

This signal can be related to \mathbf{M} at the center of a pickup-loop ($z = 0$), in the excitation coil direction \hat{z} , and the radius of the pickup loop R_{pl} by

$$\mathbf{A}_{\text{sc}}(r = R_{\text{pl}}, z = 0) = \frac{\mu_0}{4\pi} \frac{M}{R_{\text{pl}}^2} \hat{\varphi}. \quad (2.1)$$

2.2 SQUID magnetometer

Based on the Josephson junction effect, the superconducting quantum interference device (SQUID) is commonly used to detect magnetic moments. We used a quantum-design MPMS3 magnetometer. The SQUID's output is a voltage proportional to the magnetic flux through the gradiometer. The output voltage of our device can be translated to units of magnetic moment with a resolution of $1 \cdot 10^{-10} \text{ A}\cdot\text{m}^2$.

The measurements can be done in two different detection methods. (I) DC scan mode. In this mode, we record the SQUID's output voltage $V(z)$ while the ring and the excitation coil move relative to the gradiometer. The DC mode allows detection of the excitation coil signal profile as well since the entire coil can be pulled out of the gradiometer. Our gradiometer detects magnetic moments within a range of 15 mm on each side of its center. This sets the length of our excitation coil. When measuring over a wide temperature range, detection of the excitation coil contribution is essential to determine the flux it generates at each temperature. ((II) VSM mode, where the ring vibrates around the center of the gradiometer with an amplitude of 5 mm. Each measurement is averaged over 2 second. The motor creates sinusoidal sample motion with a frequency f . Average voltage output is obtained by Lock-in detection at a $2f$ signal. In this mode, the excitation coil does not contribute to the signal significantly. The VSM mode is fast and allows fine temperature scans without needing to achieve temperature stability at each measuring point. Another advantage is that the nulling of the external field is best in a range of 10 mm to each side. Hence, the sample remains in the nulled field range during the measurement.

The best way to understand the signal in a measurement of the Stiffnessometer, as illustrated in Fig. 2.1(c), is to look at the raw data of a DC scan. A typical DC mode measurement is demonstrated in Fig. 2.2. The red symbols represent the excitation coil signal moving through the gradiometer at $T > T_c$. Before the lower end of the excitation coil has reached the gradiometer, the flux through it is zero. When the lower end of the excitation coil transverse the gradiometer, its contribution to the total flux changes from zero to positive to negative and back to zero. The upper end of the excitation coil has the opposite effect; Its contribution to the flux goes from zero to negative to positive and back to zero. But there is a time (or distance) delay between the lower-end and upper-end contributions, leading to the observed signal.

At $T < T_c$, the ring adds its own signal, as shown by blue symbols in Fig. 2.2. The ring produces a current that generates opposite flux to the one of the excitation coil. The ring signal is concentrated on a narrower range on the z axis. By subtracting the

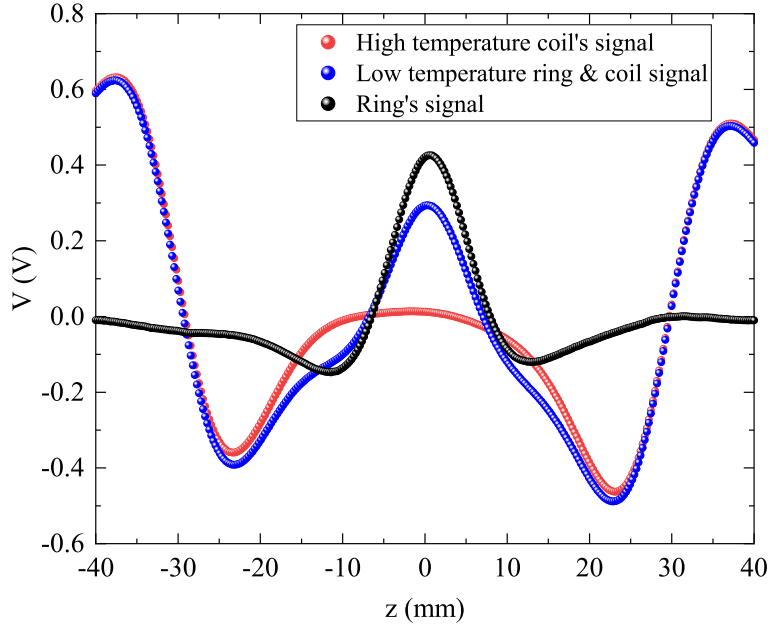


Figure 2.2: A typical DC measurement of a ring in the center of an excitation coil is scanned using a gradiometer connected to a SQUID. At high-temperature when the ring is not superconducting (in red symbols); At low-temperature when the ring is superconducting (in blue symbols); and in black symbols, the difference between these measurements. This is a measurement of a LSCO ring with a current of 3 mA in the excitation coil. It was taken from [12] and measured in a Cryogenic SQUID.

high-temperature measurement from the low-temperature one, it is possible to remain with ring's signal alone, as demonstrated by the black symbols.

Chapter 3

Measurements

3.1 Stiffness

We cool the system to a certain temperature below T_c with zero current in the excitation coil. After the temperature has stabilized, we gradually increase the current in the excitation coil while measuring the superconducting magnetic moment. An example of measurement at $T = 12$ K is presented in the inset of Fig. 3.1(a). A repetition of this process at different temperatures appears in panel (a). To isolate the superconducting signal, we subtract the moment of the measurement with zero current, which is due to the ferromagnetic properties of FeSeTe, not its stiffness. In addition, we remove the current dependence of the signal above T_c . This signal is due to the excitation coil's finite length and asymmetry.

Typical behavior in our measurements is a linear relation between the ring's moment and the excitation coil current, for low currents, as expected (see Ref. [13] and Sec. 4.1). At some value of current, the linear relation breaks. This value defines the critical current in the ring I_c . From that point on, the moment is expected to stop growing with the increasing current and reach a saturation. In our measurement, beyond the breakpoint, the magnetic signal drops sharply instead of the saturation behavior [12, 14]. This drop is caused by heat produced by the copper excitation coil, which leads to a temperature gradient between the ring and the thermometer. In fact, when the moment drops to zero, the ring has passed its critical temperature and stops being superconducting. A simple solution to this heating problem could have been to use a superconducting coil, but the T_c of FeSeTe is higher than any commercially available superconducting wire. Instead, we calibrated the temperature at the ring position using an open ring. The calibration is discussed in Appx. C.

To extract the stiffness, we fit each $M(I_{ec})$ to a line in a temperature-dependent range due to the variation in the critical current. Such a fit is demonstrated in the inset of Fig. 3.1(a). The slope represents dM/dI (in the limit $I_{ec} \rightarrow 0$). The temperature dependence of the slopes appears as blue circles in Fig. 3.1(b). The measurements do not cover all the temperature range up to T_c since defining a linear region in the $M(I_{ec})$

data becomes exceedingly difficult. Nevertheless, at a temperature slightly below T_c , a knee appears in the $(dM/dI)(T)$. For a detailed discussion on the knee, see Appx. D.

The red down triangles measure $M/I(T)$ at constant $I_{ec} = 10$ mA. At $T > 13.45$ K, this current is above I_c . Such measurements cannot be used to extract the stiffness above that temperature. On the other hand, such measurement can be carried out all the way to T_c . Interestingly, the knee is observed with this constant current measurement as well. It is important to mention that the knee was detected in other FeSeTe rings (Fig. D.2).

Finally, in the inset of Fig. 3.1(b), we present the critical currents in the excitation coil, corresponding to the moment's maximum, as a function of the calibrated temperature. The large error bars at the low temperatures range are due to the large current in the coil, leading to a strong temperature gradient and uncertainty in the temperature calibration.

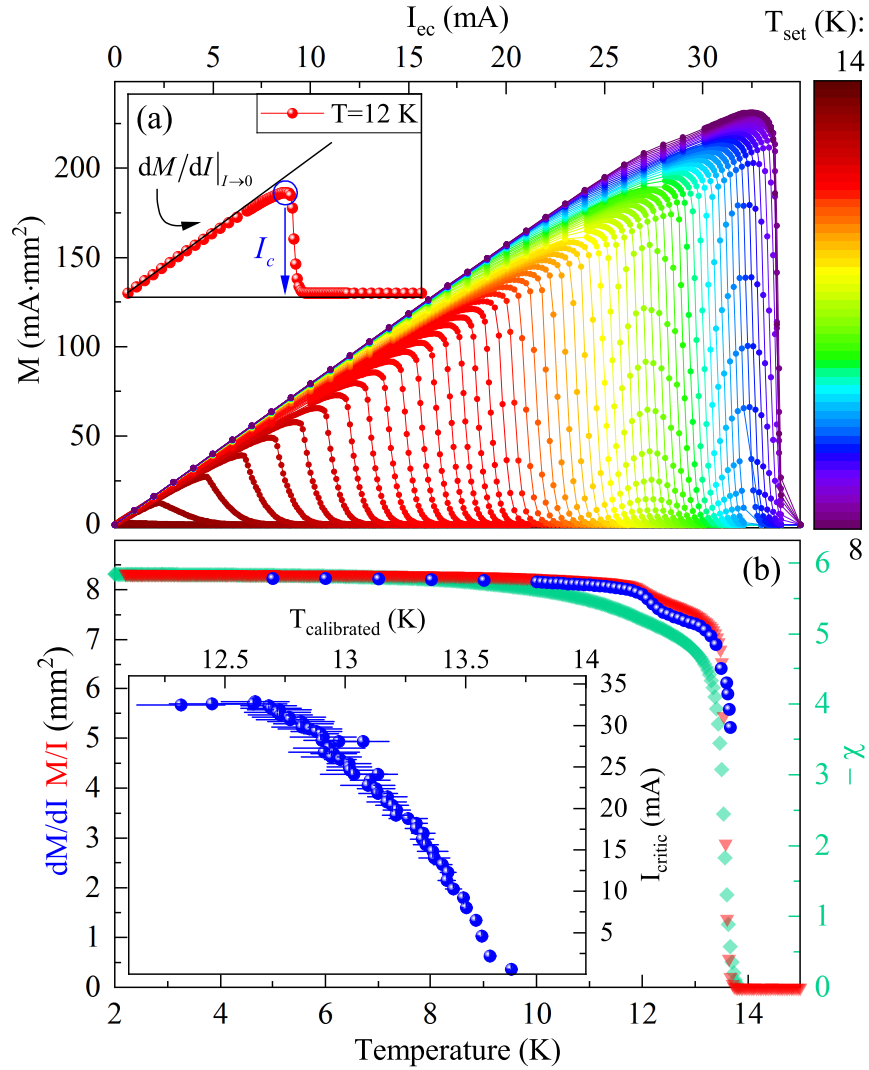


Figure 3.1: (a) Stiffness measurements. Superconducting magnetic moment vs. the current in the excitation coil at different temperatures, indicated by the colors. The inset is focused on measurement at 12 K. A linear relation is found for low currents. At some critical current value, the signal drops to zero. The blue circles in (b) depict the temperature dependence of the linear slope obtained at low currents (far from I_c) in panel (a). (b) Critical temperature. Superconducting moment over current of the excitation coil vs. the temperature (red down-triangles) as described in Sec. 3.1; Measured susceptibility (with a minus sign) vs. the temperature (emerald diamonds) in MKS units, in the presence of a magnetic field of 1 mT, and without an excitation coil (according to Sec. 3.2). Inset (b) shows the critical currents extracted from the breakpoints in panel (a) vs. the calibrated temperature.

3.2 Susceptibility

The emerald diamonds in Fig. 3.1(b), depict the temperature dependence of the measured, zero-field cooled (ZFC) susceptibility $\chi = M/(HV_{\text{ring}})$, with a field of $\mu_0 H = 0.98$ mT parallel to the axial direction of the ring; V stands for the ring's volume. The specific susceptibility is related to the measured one by

$$\chi = \frac{\chi_0}{1 + D\chi_0}, \quad (3.1)$$

where D is the demagnetization factor, and χ_0 is the specific susceptibility. For a ring with our geometry [15], the demagnetization factor equals $D = 0.6$, and if we consider the inner radius of the ring $r_{\text{in}} \rightarrow 0$, since in ZFC, it is hard for the field to penetrate the ring hole, $D = 0.7$. With these D values (considering the effective volume of the ring in the latter case), we obtain, at $T \rightarrow 0$, $\chi_0 = -1.30$, and $\chi_0 = -1.15$, respectively. Whereas $\chi_0 = -1$ is expected in the case that all of the ring's volume is superconducting. The extra 15% in χ_0 is not clear to us. It means that our sample is not exactly a ring and therefore, we do not know D exactly. Nevertheless, it indicates that the entire sample is superconducting. A sharp transition of $\chi(T)$ is obtained toward the critical temperature, $T_c = 13.75$ K, which indicates the quality of the material. Interestingly, in magnetization measurements, the knee is not observed (In other rings it does appear Fig. D.2(b)).

3.3 Hysteresis loop

To characterize the magnetic properties of the FeSeTe sample, we performed a magnetic hysteresis loop measurement, which is depicted in Fig. 3.2(a). This measurement is done above the critical temperature, at $T = 15$ K. We first increase the field from zero to 2 Tesla while measuring the magnetic moment, then decrease it to -2 Tesla and back to zero. The opening of a hysteresis loop is an indication of ferromagnetism. Another sign is that the moment of the first point, at $H = 0$, is different from zero. It might be difficult to notice this in the figure. However, this feature makes it possible to detect the sample without applying fields or currents above and below T_c in contrast to non-magnetic materials. Additional properties that can be deduced from this measurement are the magnetization saturation, retentivity (remanence), and coercivity values: $M_{\text{sat}} = 1.58$ A·mm², $M_{\text{remanence}} = 0.22$ A·mm², and $\mu_0 H_{\text{coercivity}} = 0.0153$ Tesla, respectively. From the magnetization saturation and the magnetic moment of a free Fe ion $m_{\text{Fe}^{++}} = 5.4\mu_B$ or $m_{\text{Fe}^{3+}} = 5.9\mu_B$, where μ_B is the Bohr magneton [16], we can deduce that the fraction of the free iron ions per unit cell in the sample is $y = 0.009$ or $y = 0.008$, respectively. Wang et al. [17], performed inelastic neutron scattering measurements of Fe_{0.98}Se_{0.5}Te_{0.5} and claimed that $m_{\text{Fe}} = 2.85\mu_B$. The corresponding value for the iron fraction is $y = 0.017$. More details about the calculation description

at Appx. A.3.

3.4 Critical magnetic fields

The response of the superconducting ring to an applied magnetic field at different temperatures below T_c is reflected in Fig. 3.2(b). From that measurement, we extract the first and second critical fields, H_{c1} and H_{c2} . H_{c1} is defined by the maximum magnitude of the moment for each temperature. A second peak emerges at an intermediate field between H_{c1} and H_{c2} , as discussed in Ref. [18]. This phenomenon is called the second peak effect and is attributed to the role of twin boundaries. In principle, H_{c2} is defined by the value of H for which $M = 0$ [19]. However, it is not easy to define H_{c2} because of the asymptotic behavior of the moment. Therefore, we chose a criterion by which H_{c2} is the field at which the moment is 10% of the second peak magnitude. Below a temperature of 10 K, H_{c2} becomes higher than the maximum field available to us. H_{c1} and H_{c2} as a function of temperature are shown in the inset of panel (b).

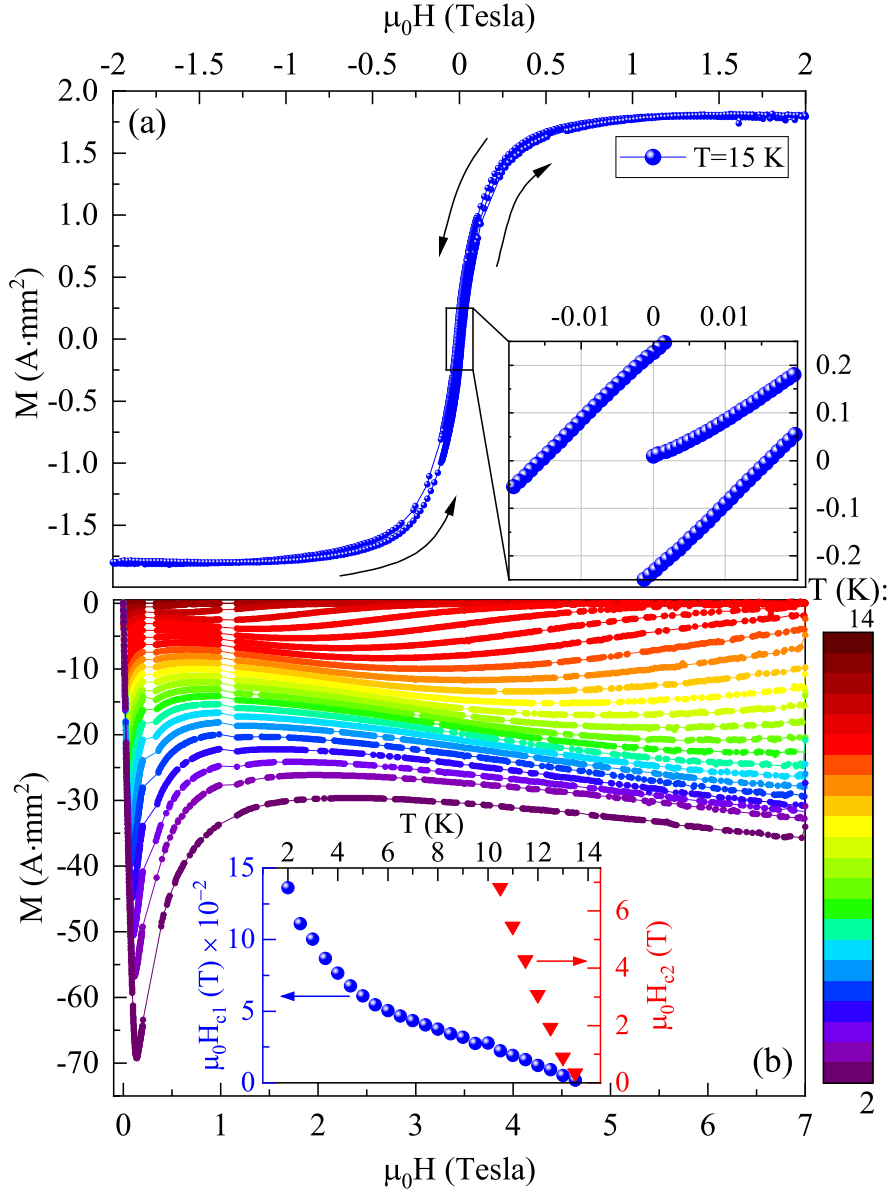


Figure 3.2: Magnetic moment vs. the external magnetic field. (a) Magnetic hysteresis loop above the critical temperature. (b) $M(H)$ at different temperature values below the critical temperature, as indicated by the colors. Inset: The temperature dependence of the critical fields H_{c1} (blue circles) and H_{c2} (red down-triangles) appear in the left and right Y-axis, respectively.

Chapter 4

Analysis Model

4.1 Stiffness

In the low flux regime (low currents in the excitation coil), the magnitude of the order parameter is constant almost all over the superconducting ring and zero outside [13]. Substituting $\mathbf{B} = \nabla \times \mathbf{A}$ and London equation into amperes law gives

$$\nabla \times \nabla \times \mathbf{A}_{\text{sc}} = -\mu_0 \rho_s \mathbf{A}_{\text{tot}}, \quad (4.1)$$

since on the ring $\nabla \times \mathbf{A}_{\text{ec}} = 0$. In the London gauge, $\nabla \times \nabla \times \mathbf{A} = -\nabla^2 \mathbf{A}$, and the vector potential outside an infinitely long coil is given by

$$\mathbf{A}_{\text{ec}}(r) = \Phi_{\text{ec}} / (2\pi r) \hat{\phi}; \quad (4.2)$$

with Eq. 1.4, we arrive at the partial differential equation (PDE)

$$\nabla^2 \mathbf{A}_{\text{sc}} = \frac{1}{\lambda^2} \left(\mathbf{A}_{\text{sc}} + \frac{\Phi_{\text{ec}}}{2\pi r} \hat{\phi} \right), \quad (4.3)$$

where $\lambda = \infty$ outside the SC. Normalizing the spatial variables and vector potential as follows

$$\mathbf{r}/R_{\text{pl}} \rightarrow \mathbf{r}, \quad \mathbf{A}_{\text{sc}}/\mathbf{A}_{\text{ec}}(R_{\text{pl}}) \rightarrow \mathbf{A}, \quad \lambda/R_{\text{pl}} \rightarrow \lambda, \quad (4.4)$$

R_{pl} is the pickup loop radius, and in cylindrical coordinates, $\mathbf{A} = A(r, z) \hat{\phi}$, we end up with the following PDE

$$\frac{\partial^2 A}{\partial z^2} + \frac{\partial^2 A}{\partial r^2} + \frac{1}{r} \frac{\partial A}{\partial r} - \frac{A}{r^2} = \frac{1}{\lambda^2} \left(A + \frac{1}{r} \right). \quad (4.5)$$

We use the finite element-based FreeFem++ software [20] to solve this PDE for different values of λ and the dimension of our FeSeTe ring, appearing in the caption of Fig. 2.1. The equation is solved in a box such that $z \in [-L, L]$, and $r \in [0, 8L]$ with $L = 8.5$ mm, which equals the R_{pl} . Dirichlet boundary conditions are imposed.

As shown in Fig. 2.1(a), the ring's outer radius is not uniform. However, according

to the theory, see Appx. A.2, in the low flux regime, the current flow in a layer of width λ near the inner rim of the ring, so the system's rotational symmetry is not severely compromised. When the flux through the ring is increased, the current layer retreats toward the outer rim. This retraction ends when the current layer reaches the outer rim. In our case, it happens at the shortest distance of the outer rim from the center. We use this distance as the outer radius in the PDE 4.5.

The red line in the inset of Fig. 5.1(a) depicts the numerical solution of PDE 4.5. The Y-axis is the normalized vector potential A at the ring's height $z = 0$, and the pickup-loop radial location $r = R_{\text{pl}}$. The X-axis is a logarithmic scale of the normalized stiffness $(R_{\text{pl}}/\lambda)^2$. Normalizing Eq. 2.1 by the vector potential of an infinite coil,

$$A_{\text{ec}}(R_{\text{pl}}) = \frac{\mu_0 n I_{\text{ec}}}{2R_{\text{pl}}} \sum_i r_{\text{ec},i}^2, \quad (4.6)$$

where n , $r_{\text{ec},i}$, and I_{ec} are windings per unit length in one layer, radius of the i^{th} layer, and current of the coil, respectively, we obtain the dimensionless vector potential

$$A(z = 0, R_{\text{pl}}) = \sum_i \frac{g}{2\pi n R_{\text{pl}} r_{\text{ec},i}^2} \cdot \frac{M}{I_{\text{ec}}}, \quad (4.7)$$

where M is the superconducting magnetic moment, and g is a calibration constant.

In reality, the coil is not infinite, and the external dimensions of the ring can be different from the actual superconductor dimensions due to cutting and drilling. Therefore, the constant calibration g is determined experimentally in two different methods: (I) We compare the saturated value of A from the solution of PDE 4.5 (the red line in Fig. 5.1(a) inset) to the saturated value of dM/dI (the lowest available temperature of the blue circles in Fig. 3.1(b)). This method cannot be used to determine $\lambda(T \rightarrow 0)$ since exactly this limit is used for the calibration. Nevertheless, it gives an estimate for g ; (II) In the second method, we use a literature value of a low temperature stiffness of similar material to predict A with the PDE solution and compare it to our measured dM/dI through Eq. 4.7 at the same temperature to extract g . For this work, the stiffness was taken from Ref. [3]. We found $g_1 = 0.5363$ and $g_2 = 0.5336$ in methods (I) and (II), respectively. We also applied the same calibration methods for a ring-shaped Niobium with similar dimensions and found $g_1 = g_2 = 0.68674(2)$ while using $\lambda(0) = 39$ nm as the literature value for Niobium [21]. Although the two calibration methods give different values for the penetration depth at low temperatures, towards T_c , the values converge and almost coalesce, as seen in the blue and emerald triangles in Fig. 5.1(c). In other words, the stiffness determined by the Stiffnessometer is not sensitive to the calibration method once dM/dI is out of the saturation region.

4.2 Coherence length

In the low flux regime $J \ll r_{\text{in}}^2/\lambda\varepsilon$ and for $\lambda \ll r_{\text{out}} - r_{\text{in}}$ and h , where h is the ring's height, and $J := \Phi_{\text{ec}}/\Phi_0$, deep inside the ring $A_{\text{tot}} = 0$, hence $A_{\text{sc}} = -A_{\text{ec}}$. For $J > r_{\text{in}}^2/\sqrt{8}\xi\lambda$, the current necessary to produce A_{sc} at r_{in} passes the local critical current [13]. Then, it is energetically preferable for the order parameter magnitude to gradually diminish in the inner rim of the ring. Consequently, the superconducting ring hole grows effectively, and effective inner radius $r_{\text{in}}^{\text{eff}}$ is established. At even higher flux, $r_{\text{in}}^{\text{eff}}$ approaches r_{out} , and the SC can no longer expel the applied flux, namely, to cancel A_{ec} . This happens when

$$J_{\text{fold}} \approx \frac{r_{\text{out}}^2}{\sqrt{8}\xi\lambda}. \quad (4.8)$$

The name "folding" means that increasing J past J_{fold} does not change A_{sc} . Therefore, it is identified with the critical applied flux $J_{\text{fold}} = \Phi_c/\Phi_0$, which is directly related to the critical current in the excitation coil. While the validity regime of Eq. 4.8 is in the limits $\xi \ll \lambda \ll r_{\text{out}} - r_{\text{in}} \ll h$, we believe it is valid for $\lambda \ll r_{\text{out}} - r_{\text{in}}$ and $\lambda \ll h$ separately.

For $J > J_{\text{fold}}$, vortices are expected to penetrate from the inner rim toward the outer one so that the superconducting moment no longer grows with amplification of the current of the excitation coil. These vortices are manifested in increases in $\nabla\phi$. A different approach to finding the relation between ξ and Φ_c appears in Appx. A.2.

Chapter 5

Data Analysis

Eq. 4.7 relates the linear slope of the $M(I)$ measurements, shown by blue circles in Fig. 3.1(b), to the numerical solution of the PDE. The blue open circles in Fig. 5.1(a)-inset represent the converted points for g_2 . Each of those points belongs to a different temperature and gives a unique stiffness value. The temperature dependence of λ for the two different g values is presented on a linear scale on the right Y-axis of Fig. 5.1(a) and of λ^{-2} on a logarithmic scale in Fig. 5.1(c). The difference between the two calibration methods is revealed in both sub-figures, but they are minute at $T \rightarrow T_c$. The linear regression towards the critical temperature on the logarithmic scale represents the critical exponent m_ρ , according to the power-law

$$\rho \propto (1 - T/T_c)^{m_\rho}, \quad (5.1)$$

with $m_\rho = 0.91 \pm 0.02$. This relation describes the data well from the knee temperature 12.4 K (blue circles in Fig. 3.1(b)) all the way to T_c .

Based on the stiffness and the critical current in the inset of Fig. 3.1(b), we extract the coherence length using Eq. 4.8 and Eq. 4.2, as depicted by the left Y-axis of Fig. 5.1(a) and on a logarithmic scale in Fig. 5.1(b). Again, we fit the data to the power-law

$$\xi^{-1} \propto (1 - T/T_c)^{m_\xi}. \quad (5.2)$$

We found $m_\xi = 0.41 \pm 0.02$, however we can not really extract a power law from this figure due to the small change in ξ in the range of validity, see Fig. 5.1(b). The deviation from the linear regression at high temperatures may be a result of analysis failure since the penetration depth is no longer much smaller than the ring's height $\lambda \ll h$. At low temperatures, we associate the deviation with heating caused by the strong current in the excitation coil. It is worth mentioning that it belongs to measurements from temperatures below the knee.

Alternative determination of ξ is from H_{c2} [19] according to the equation

$$\mu_0 H_{c2} = \frac{\Phi_0}{2\pi\xi^2(T)}. \quad (5.3)$$

ξ is presented on a linear scale with black squares on the left Y-axis of Fig. 5.1(a) and $1/\xi$ on a logarithmic scale in panel (b) of the same figure for comparison. Here we also fit the data according to Eq. 5.2 and obtained $m_\xi = 0.60 \pm 0.03$.

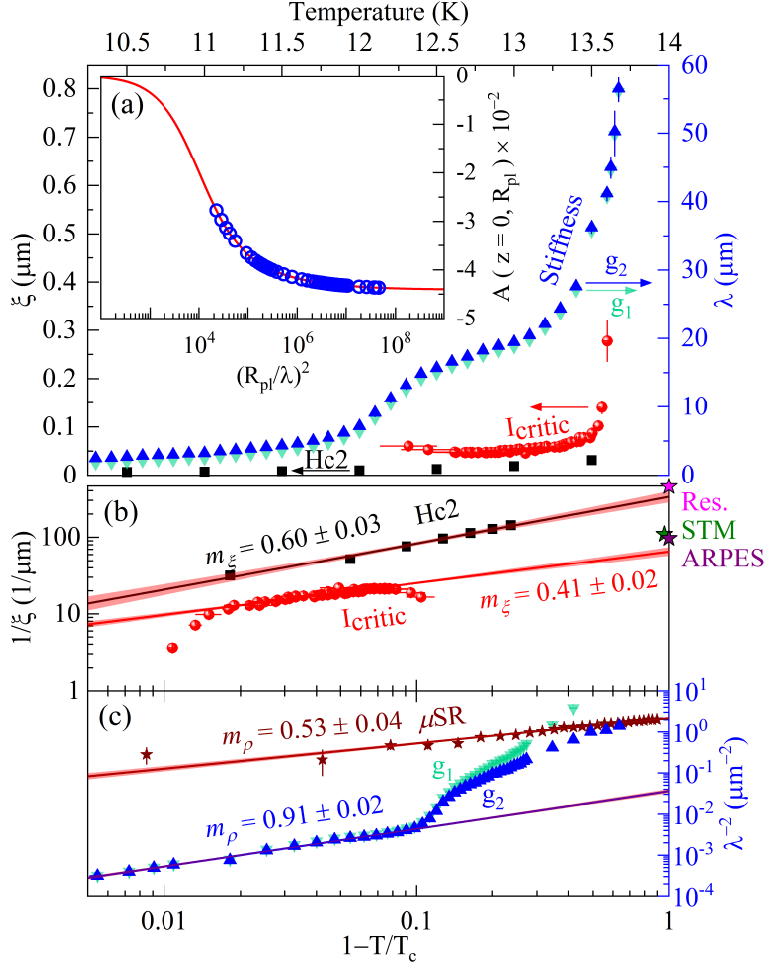


Figure 5.1: Penetration depth and coherence length. The red line in inset (a) depicts a semi-log plot of the numerical solution of the PDE 4.5, namely, the normalized vector potential evaluated at the pickup-loop radius and $z = 0$ for different values of $(R_{pl}/\lambda)^2$. The blue open circles represent the linear slopes in Fig. 3.1(b) through Eq. 4.7. (a) The penetration depth as a function of the temperature in blue and emerald for the different calibration methods. The left Y-axis shows the temperature dependence of the coherence length, in red from the critical current measurement in Fig. 3.1(b)-inset through Eq. 4.8 with the measured λ and in black squares measurements from the second critical field in Fig. 3.2(b)-inset with Eq. 5.3. (b) and (c) panels are log-log plots of $1/\xi$ and the stiffness λ^{-2} vs. $1 - T/T_c$, respectively. The linear regression represented the critical exponents according to Eq. 5.1 and Eq. 5.2, respectively. For comparison, we add to (b) measurements (stars shaped) of $1/\xi$ from the resistivity method [10] in magenta, ARPES [9] in purple, and STM [8] in green. The brown stars in (c) are μ SR measurements of the stiffness [3]

Chapter 6

Discussion and Conclusion

6.1 Comparison with theory

Gavish et al. [13] considered an infinitely long excitation coil pierces a hollow superconducting cylinder confined to the region $0 < r_{\text{in}} < r < r_{\text{out}}$. The dimensionless Ginzburg-Landau (GL) free energy is read as

$$\mathcal{F} = \frac{1}{2} \int_{\mathbb{R}^3} \lambda^2 \xi^2 |\nabla \times \mathbf{A}|^2 d\mathbf{x} + \frac{1}{2} \int_{\text{sc}} \left[\xi^2 |\nabla \phi|^2 + \xi^2 \psi^2 |\mathbf{A} - \nabla \phi|^2 + \frac{1}{2} \psi^4 - \psi^2 \right] d\mathbf{x}, \quad (6.1)$$

where $\Psi = \psi e^{i\phi}$, and the total vector potential is given by $\mathbf{A} = A(r) \hat{\phi} = [A_{\text{sc}}(r) + A_{\text{ec}}(r)] \hat{\phi}$. The spatial variables, vector potential, and order parameter are normalized according to

$$\mathbf{x} \rightarrow \frac{\mathbf{x}}{R_{\text{pl}}}, \quad \mathbf{A} \rightarrow \frac{\mathbf{A}}{A_0}, \quad \psi \rightarrow \frac{\psi}{\psi_\infty}, \quad (6.2)$$

where

$$A_0 = \frac{\phi_0}{2\pi R_{\text{pl}}}, \quad \phi_0 = \frac{2\pi \hbar c}{e^*}, \quad \psi_\infty = \sqrt{-\frac{\alpha}{\beta}}. \quad (6.3)$$

ξ , and λ (in this section) are the normalized coherence length and penetration depth are related to each other by

$$\lambda^2 = \xi^2 \cdot \frac{\beta m^{*2} c^2}{2\pi \hbar^2 e^{*2}}. \quad (6.4)$$

The GL equations are obtained by minimizing the free energy variation with respect to ψ , and A_{sc} , respectively:

$$\xi^2 \left(\psi''(r) - \frac{\psi'(r)}{r} \right) = \psi^3(r) - \left(1 - \xi^2 \left(A_{\text{sc}}(r) + \frac{J - m}{r} \right)^2 \right) \psi(r), \quad (6.5)$$

and

$$A_{\text{sc}}''(r) + \frac{A_{\text{sc}}'(r)}{r} - \frac{A_{\text{sc}}(r)}{r^2} = \frac{1}{\lambda^2} \left(A_{\text{sc}}(r) + \frac{J - m}{r} \right) \psi^2(r), \quad (6.6)$$

where $\mathbf{A}_{\text{ec}} = J/r \hat{\phi}$, $J = \Phi/\Phi_0$, and Φ is the flux inside the coil.

β is taken to be temperature independent, so it inferred from Eq. 6.4 that $\rho \propto$

$(\xi^{-1})^2$. Therefore, under GL it is expected that

$$m_\rho/m_\xi = 2, \quad (6.7)$$

where m_ρ and m_ξ are defined in Eq. 5.1 and Eq. 5.2, respectively. From the Stiffnessometer technique, we obtain

$$m_\rho/m_\xi = 2.22 \pm 0.12. \quad (6.8)$$

This ratio could be compared with measurements done in an applied field. In Fig. 5.1(c), we show the penetration depth taken by μ SR [3]. The μ SR stiffness values close to T_c differ from those determined by the Stiffnessometer. Moreover, the power-law value $m_\rho^{\mu\text{SR}} = 0.53 \pm 0.04$ is different by nearly a factor 2 from the Stiffnessometer. Even worse, the μ SR measurements are done in a fixed magnetic field, which becomes higher than H_{c2} as one approaches T_c . As mentioned before, the discrepancy between μ SR and the Stiffnessometer could also result from an interaction between the applied field and the underline ferromagnet.

Similarly, compared to the Stiffnessometer measurements, the values of ξ obtained by the H_{c2} method are lower by a factor of 0.37 (at $T = 13$ K), and the power-law (of $1/\xi$) is higher by 0.2. The result obtained from the μ SR and H_{c2} methods gives $m_\rho^{\mu\text{SR}}/m_\xi^{H_{c2}} = 0.88 \pm 0.08$, very far from the GL expected value.

The first critical field, H_{c1} , is related to λ and ξ [22] via

$$\mu_0 H_{c1} = \frac{\Phi_0}{4\pi\lambda^2} \ln \frac{\lambda}{\xi}. \quad (6.9)$$

Since we already found all of these properties, we tried to get some closure in different ways, without success: I) Calculating λ using ξ from H_{c2} (Fig. 3.2(b)-inset red symbols and Eq. 5.3) and H_{c1} (Fig. 3.2(b)-inset blue symbols). The values obtained for λ at $T/T_c = 0.76$ is 13 times greater than the stiffnessometer's value and 7 than the μ SR value; II) Finding H_{c1} at $T = 0$ using λ from μ SR and ξ from STM. We get $H_{c1}(0) = 1.5$ mT, which is 100 times smaller than the measured at 2 K.

Bendele et al. [4], addressed this problem by considering demagnetization factor D . They introduced

$$B = \mu_0 (M/V + H_{\text{int}}), \quad (6.10)$$

where $H_{\text{int}} = H_{\text{ext}} - DM/V$. H_{int} and H_{ext} are the internal and applied field, respectively, $\mu_0 H_{c1} \rightarrow B$ in Eq. 6.9. This calculation is very sensitive to the ring's volume and D accuracy. In Sec. 3.2 we consider two options for D . If we adopt the disk option get a much smaller B than measured (as expected). If we consider the ring option we find a negative B value. Sometimes additional constant is considered in Eq. 6.9 that includes the effect of the hard core of the vortex line [4, 23, 24], but in our case, its effect is negligibly.

For further comparison, low-temperature measurements of $1/\xi$ from other methods have been added to Fig. 5.1(b) (stars shaped). Resistivity [10] in magenta, ARPES [9] in purple, and STM [8] in green. The resistivity measurement is, in fact, an H_{c2} measurement and, the result obtained is close to the one we get from the magnetization method ($\xi_{H_{c2}}/\xi_{\text{Res}} = 1.6$ at $T = 0$). In ARPES they find Fermi velocity over gap ξ_0 . This is related to the GL ξ at $T = 0$, $\xi(0)$, by a factor of 0.74. The same factor was taken into account in the STM measurement. Unlike the H_{c2} measurements, the results from the other two methods are closer to the linear regression of the Stiffnessometer method ($\xi_{\text{Stiff}}/\xi_{\text{ARPES}} = 1.7$ and $\xi_{\text{Stiff}}/\xi_{\text{STM}} = 1.9$ at $T = 0$).

6.2 Conclusion

We developed a method, ideal for magnetic superconductors close to T_c , to measure both the penetration depth λ and coherence length ξ . For FeSeTe we find that λ and ξ are longer than previously thought. In addition, their temperature dependence agrees better with the GL predictions. A second transition, that looks like a knee, is observed at temperature below T_c in the stiffness measurements. We could not rule out the possibility that this transition is due either to nematic order, surface superconductivity, multiple Fermi surfaces, or a simple geometrical effect.

Appendix A

Mathematical Description

A.1 London equation derivation

The London equation gives the relation between a superconducting current density and the electromagnetic fields in and around a superconductor. Let us consider an infinitely long excitation coil pierces a superconducting ring. When the current in the coil is set to a finite value, the magnetic field outside the coil is zero, but there is a rotor-free vector potential outside, which is proportional to its current. We use the Maxwell-Faraday equation,

$$\nabla \times \mathbf{E} = -\frac{\partial \mathbf{B}}{\partial t} = -\nabla \times \frac{\partial \mathbf{A}}{\partial t}, \quad (\text{A.1})$$

where $\mathbf{B} = \nabla \times \mathbf{A}$. By integrating we get

$$\mathbf{E} = -\frac{\partial \mathbf{A}}{\partial t} + \nabla \mathcal{V}, \quad (\text{A.2})$$

where \mathcal{V} is a scalar function. We choose it to be as follows

$$\nabla \mathcal{V} = \frac{\hbar}{e^*} \nabla \frac{\partial \phi}{\partial t}, \quad (\text{A.3})$$

where e^* is the charge of the particles. Substituting the expression above into Eq. A.1

$$\mathbf{E} = -\frac{\partial}{\partial t} \left(\mathbf{A} - \frac{\hbar}{e^*} \nabla \phi \right). \quad (\text{A.4})$$

In a superconductor, there is zero resistivity. Hence, the acceleration of the charges is dictated by $m^* \dot{\mathbf{v}} = e^* \mathbf{E}$, where m^* is the charge carrier's mass. Integrating over time to get the velocity

$$\mathbf{v} = -\frac{e^*}{m^*} \int \frac{\partial}{\partial t} \left(\mathbf{A} - \frac{\hbar}{e^*} \nabla \phi \right) dt. \quad (\text{A.5})$$

For a thin ring, the velocity is only in the azimuths direction, and by the system's symmetry, the vector potential and the velocity are independent in $\hat{\phi}$. Thus, there is no difference between ∂t and dt , and the integral in the equation above is canceled.

In addition, we use the definition of the charge current density $\mathbf{j} = e^*|\psi|^2\mathbf{v}$, with the identification $n_s^* = |\psi|^2$, to obtain the gauge-invariant London equation (same as Eq. 1.1)

$$\mathbf{j} = -\rho_s\left(\mathbf{A} - \frac{\Phi_0}{2\pi}\nabla\phi\right), \quad (\text{A.6})$$

where n_s^* is the charge carrier's density, the stiffness ρ_s is defined in Eq. 1.2, and Φ_0 is the flux quanta. It is essential to mention that the London equation is much more durable than in this description. It does not depend on whether we cool the sample and then turn on the current or vice versa. Additionally, it is more general than this specific setup and geometric.

A.2 Coherence length – approximate theory

This time, we consider an infinitely long excitation coil that pierced a long and thin superconductive cylinder. The system can be described by the Ginzburg-Landau (GL) free energy (Eq. 6.1). The GL equations are obtained by minimizing the free energy with respect to the vector potential generated by the SC A_{sc} and the normalized order parameter magnitude ψ separately Eq. 6.5 and 6.6. The solution of the GL equations shows how ψ and A_{sc} arranges in the sample and how they evolve when we increase the flux throw the hole. Gavish et al. [14] solved these equations in different flux regimes and found that for low flux $\psi = 1$ almost all along the sample. But, when the flux is increased, ψ will retreat toward the outer radius of the cylinder. When it reaches the outer radius, and we keep increasing the flux, ψ will no longer be one anywhere, and the system's rigidity will break. That point defines the critical flux inside the ring.

The solution of the GL equations also relates the transition radius of ψ to the current loop radius. For low flux, the current flow mostly in a boundary layer of width λ from the inner rim of the cylinder (see Fig. A.1(a)). Deep inside the superconducting cylinder, there is no current density j or magnetic field. Hence, according to the London equation (Eq. 1.3), $A_{tot} = A_{ec} + A_{sc} = 0$ means that the applied flux Φ_{ec} must be balanced by the flux generated by j , which flows at a width λ near the inner rim,

$$\Phi_{sc} = \mu_0 j \lambda \pi R_{in}^2. \quad (\text{A.7})$$

When the flux is increased, the inner rim becomes normal, and the current retreats into the sample and flows in a layer of width λ , see Fig. A.1(b). But still, it has to balance the applied flux in the superconducting region (beyond the current layer),

$$\Phi_{sc} = \mu_0 j \lambda \pi R_{eff}^2. \quad (\text{A.8})$$

The flux for which the current layer reaches the outer rim of the cylinder is identified

as the critical flux and the critical current density accordingly, see Fig. A.1(c),

$$\Phi_c = \mu_0 j_c \lambda \pi R_{\text{out}}^2. \quad (\text{A.9})$$

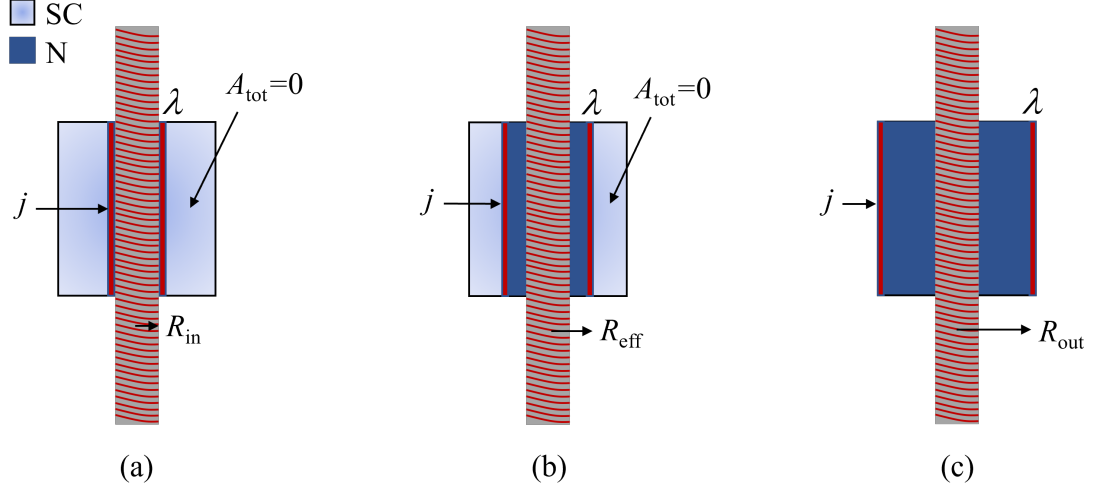


Figure A.1: Illustration of the evolution of the current density in a superconducting cylinder with the increase of flux through the hole. Superconducting region in light blue and normal in dark blue. (a) Low flux; (b) intermediate flux; and (c) strong flux.

The current definition is

$$j = e^* |\psi|^2 v = \frac{e^{*2} |\psi|^2}{m^*} \frac{1}{e^*} m^* v = \frac{1}{\mu_0 \lambda^2} \frac{1}{e^*} m^* v, \quad (\text{A.10})$$

where in the second equality we used Eq. 1.2, and 1.4. We use the connection between the critical momentum and the coherence length, $m^* v_c = \hbar / \sqrt{3} \xi$, from Tinkham [19] (equation 4.37) and plug it into the current definition to get the critical current

$$j_c = \frac{1}{\mu_0 \lambda^2} \frac{1}{e^*} \frac{\hbar}{\sqrt{3} \xi} = \frac{1}{2\pi \mu_0 \lambda^2} \frac{\Phi_0}{\sqrt{3} \xi}, \quad (\text{A.11})$$

where $\Phi_0 = 2\pi \hbar / e^*$ is the flux quantum. We combined it with Eq. A.9 to get the expression for the coherence length,

$$\xi = \frac{1}{2\pi \mu_0 \lambda^2} \frac{\Phi_0}{\sqrt{3} j_c} = \frac{R_{\text{out}}^2}{\sqrt{12} \lambda} \frac{\Phi_0}{\Phi_c}. \quad (\text{A.12})$$

A numerical calculation of the GL equations [13] gives

$$\xi = \frac{R_{\text{out}}^2}{\sqrt{8} \lambda} \frac{\Phi_0}{\Phi_c}. \quad (\text{A.13})$$

A.3 Free iron ions in the sample

Let us assume that iron atoms that are part of a unit cell of the FeSeTe crystal do not contribute to the magnetic signal, and the contribution of the Se/Te ions is negligible. Then the total magnetic signal is caused only by the free iron ions. When the field is increased, and all the free ions are polarized in the same direction, the moment reaches a saturation M_{sat} , see Fig. 3.2(a). Consequently, the total number of free iron ions is $N_{\text{free Fe}} = M_{\text{sat}}/M_{\text{Fe}}$, where M_{Fe} is the magnetic moment of one iron ion. The mass of a unit cell is calculated from the sum of its components $m_{\text{cell}} = 2m_{\text{Fe}} + m_{\text{Se}} + m_{\text{Te}}$. The number of unit cells is obtained by dividing the ring's total mass by the mass of one unit cell $N_{\text{cell}} = m_{\text{ring}}/m_{\text{cell}}$. By partitioning the total number of free iron ions by the number of unit cells in the sample, we obtain the fraction of the free iron ions in the crystal $y = N_{\text{free Fe}}/N_{\text{cell}}$.

Appendix B

Gradiometer

The gradiometer comprises three winding groups, see Fig. 2.1(c). The two outer contain two loops each, wound clockwise, whereas the inner contains four loops wound anticlockwise. In that way, we separate the magnetic signal generated by the sample from any other field uniform in space, even if it drifted in time. The gradiometer is connected to a SQUID. The output is a voltage proportional to the difference between the flux threading the different winding groups of the gradiometer $\Phi_{\text{tot}} = -2\Phi(z - 8) + 4\Phi(z) - 2\Phi(z + 8)$, where Φ is the flux that goes through each loop, z is the location of the sample relative to the center of the gradiometer, and 8 mm is the distance between each winding group. The flux Φ depends on the distance between the sample and the loop. The proportionality between the output voltage and the magnetic moment of the sample is found once or verified by a known magnetic calibration sample.

Appendix C

Temperature calibration

Due to the heat produced by the current in the excitation coil, a temperature gradient is developed between the ring and the thermometer, s.t., the actual temperature of the sample T , and the temperature recorded by the chamber thermometer T_{ch} are not the same. Our goal is to determine the sample temperature T corresponding to each critical current I_c based on the chamber temperature T_{ch} .

The calibration process is done by measuring the temperature dependence of the magnetic moment in the presence of an applied field of $\mu_0 H \approx 1$ mT (ZFC), similarly to Sec. 3.2. However, this time we use a disconnected FeSeTe ring and repeat that measurement for different currents in the excitation coil. The critical current values from Fig. 3.1(b)-inset have been chosen to improve the accuracy.

The current in the excitation coil heats the sample but cannot generate a persistent current in the ring due to the disconnection. Nevertheless, there are three additional contributions of the excitation coil current to the signal, and all are consequences of its finite length. A good way to understand them and get an intuition is to look at the excitation coil signal that appears in figure 2-inset in Ref. [12] and by the red symbols in Fig. 2.2: I) The second-order gradiometer is insensitive to any field uniform in space, but even around its center, the excitation coil signal is not totally uniform; II) A global shift of the moment due to asymmetry of the coil (e.g., wires enter the coil from one side only). The contribution from these two sources is identified from the measurement above T_c . The measurement results after this reduction appear in Fig. C.1(a); III) A field's leakage from the excitation coil parallel to the applied field, altering the entire field in the sample and the sample's moment accordingly, as will be discussed later.

Once these shifts were eliminated, we search for the temperature correction, ΔT , for which $M(I_{\text{ec}}, T_{\text{ch}} + \Delta T)$ collapses onto the one without the current $M(0, T)$ at the steepest part of the measurement's slope as seen in Fig. C.1(b) and Fig. C.2-inset. It could also be seen that although the collapse happened close to T_c , the correction is suitable for a wide range of temperatures.

After the temperature correction, for each current, we compare the measurement with the current to the one without. The error in the temperature correction is es-

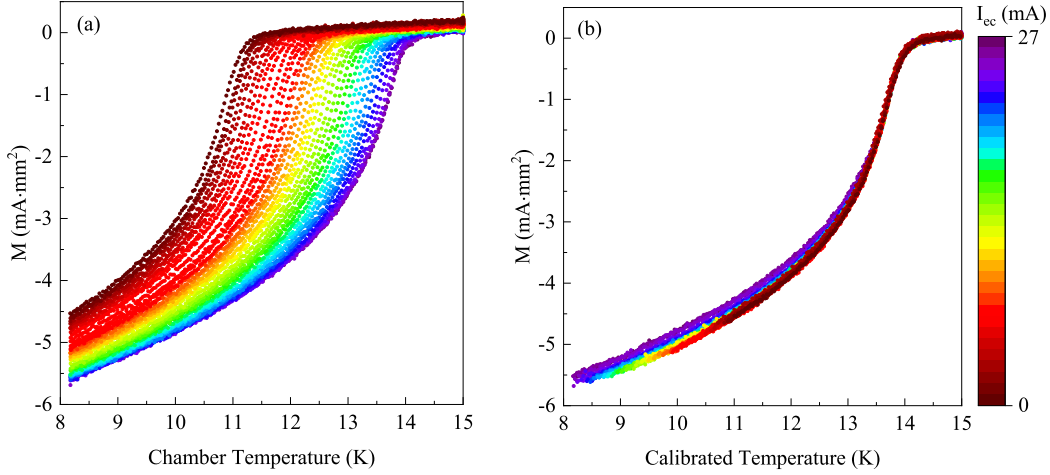


Figure C.1: Temperature dependence of the magnetic moment of a disconnected FeSeTe ring in the presence of a magnetic field, repeated for different currents in the excitation coil, as indicated by the colors. (a) Before the calibration. (b) After calibration.

timated by the temperature difference between points with the same moment value from both measurements. An example appears in Fig. C.3. The errors depend on the current in the coil and temperature. Finally, in blue circles in Fig. C.2, we present the SC critical current I_c as a function of the calibrated temperature T with error-bars.

Looking at the low-temperature range in Fig. C.1(b), we can see the moments drop as we increase the current in the excitation coil. A possible explanation is that a magnetic field is leaking from the coil. This leakage could be partially canceled by measuring the moment with both current directions, as presented in Fig. C.4(a). Indeed, the gap increases with the current while the zero current measurement stays in the middle. Averaging over both directions reduces the deviation, as in Fig. C.4(b). Notably, the magnitude of the field leaking from the coil at 10 mA current is estimated to be 0.03 mT.

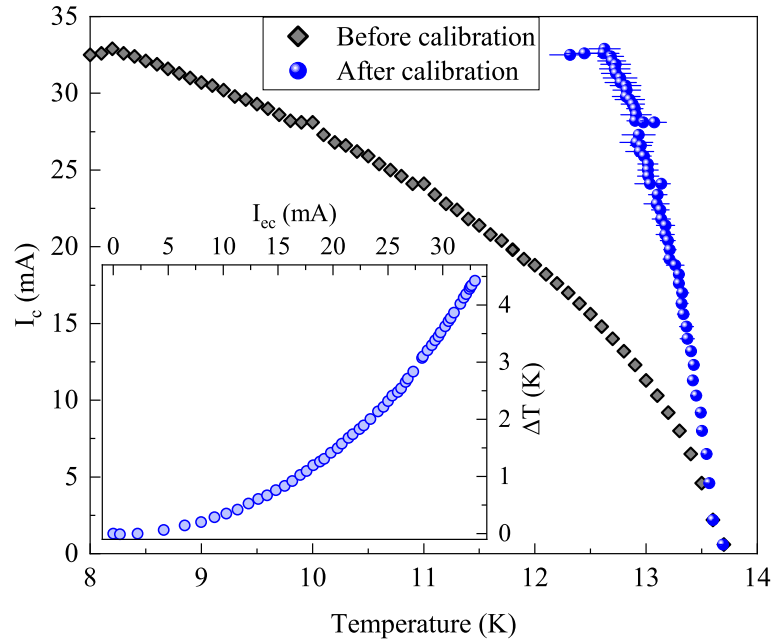


Figure C.2: Critical current inside the ring vs. the temperature. Before the calibration in gray diamonds and after in blue circles. The inset shows the temperature correction ΔT vs. the current in the excitation coil. A parabolic relation is obtained (approximately).

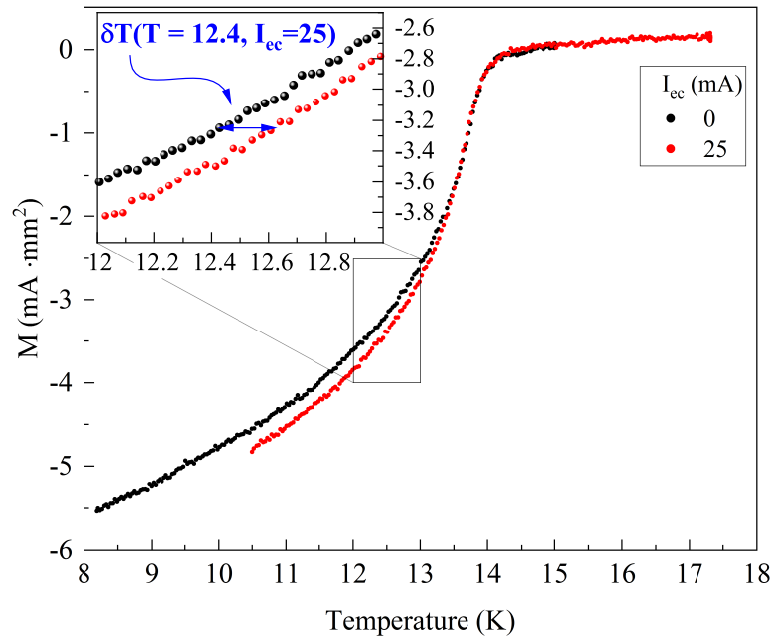


Figure C.3: Estimation of the errors in the temperature calibration process. Measurements after temperature calibration (from Fig. C.1(b)) without current in the excitation coil in black symbols and with a current of $I_{cc} = 25$ mA in red. The error is estimated by the temperature difference between two points with the same moment value. It is represented by δT and depends on the current and the temperature.

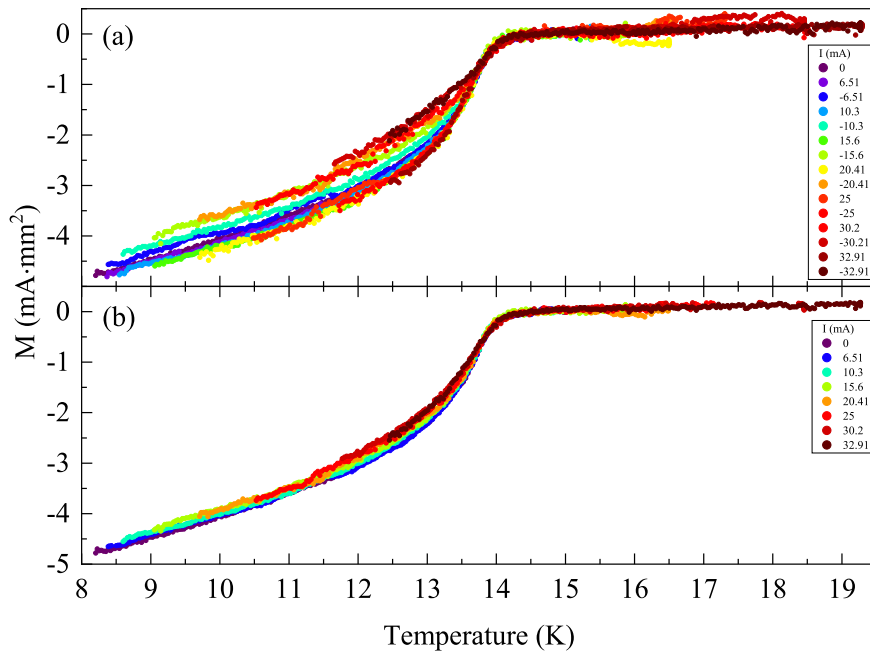


Figure C.4: Moment vs. temperature. The influence of the leaking field from the excitation coil on the measurement. (a) Calibrated measurements in the presence of positive and negative current values. (b) Averaging over the directions of the currents in (a).

Appendix D

Knee Investigation

D.1 Applied field influence

The Knee origin is still unknown, but here we present our investigation. The fact that the knee appears in measurements with the coil but not with an external field (emerald diamonds in Fig. 3.1(b)) raised the question of whether the field destroys the knee. To answer that, we'll do the following manipulation. We measure the superconducting magnetic moment vs. the temperature in the presence of a perpendicular applied field (ZFC) and current in the excitation coil as presented in Fig. D.1. In one measurement (in black), we applied a magnetic field and current in the coil, and in the second (in red) with field only. Then, we subtracted the measurement with the field from the combined one, so we left "only" with the contribution of the coil (in blue). Panel (b) of the same figure is zoomed in on the manipulated measurement (in blue), It is possible to see that the knee has not disappeared and appears at the same temperature as in the measurement with current only (in brown), as indicated by the red line.

It can be seen in Fig. D.1(b) that the saturation value (the moment at low temperatures) in the brown measurement is different from the manipulated one. This difference is due to the differences between the black and red measurements.

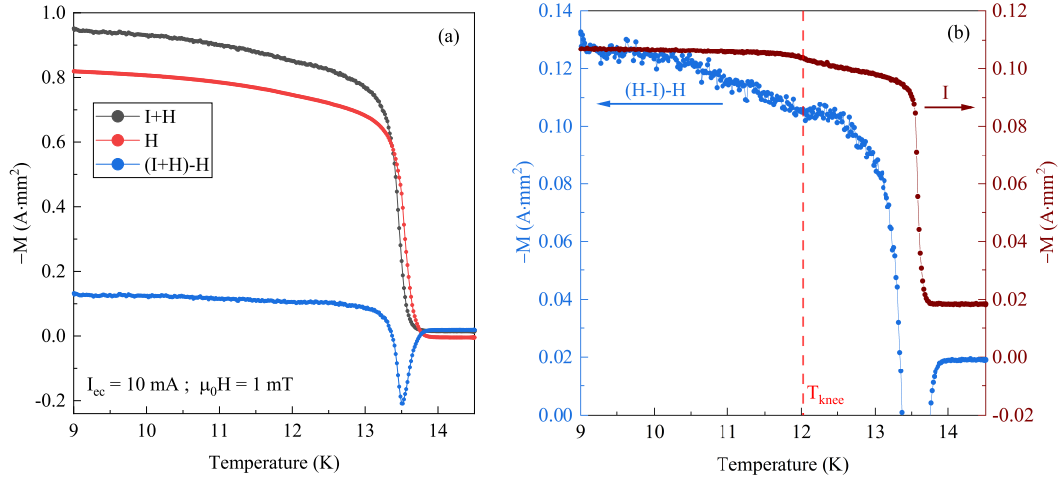


Figure D.1: Superconducting magnetic moment vs. the temperature in the presence of applied field (1 mT) and current in the excitation coil (10 mA). The blue symbols belong to the measurement in black minus the one in red. (b) Zoom in on the manipulated measurement (in blue). The brown measurement is done with a zero field and a current in the excitation coil. A shift has been inserted to the Y-axis to emphasize the knee.

D.2 Rings comparison

A comparison between different rings from different crystals appears in Fig. D.2, which shows the normalized superconducting moment as a function of the temperature. Panel (a) with a current in the excitation coil and panel (b) with an applied field. The applied currents and fields are in the range [5, 10] mA and [0.1, 3] mT, respectively, But not necessarily equal. Ring 1 is the central ring of this research. Its data appears in the red down-triangles in Fig. 3.1(b). Rings 1 and 2 are from the same crystal, 3 and 4 were measured by Eran Gazit (a former MSc student of Amit Keren) in a Cryogenic SQUID.

The knee temperature varies from ring to ring (Fig. D.2(a)), and in rings 2 and 5, do not exist at all. In panel (b), interestingly, a knee appears in the measurement of ring 3.

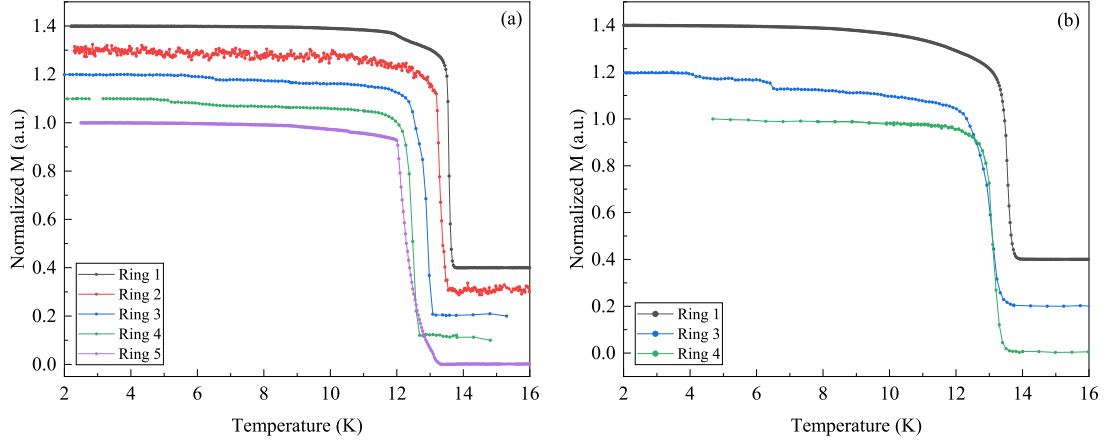


Figure D.2: Normalized magnetic moment vs. the temperature for different rings. (a) in the presence of current in the excitation coil, as described in Sec. 3.1. (b) in the presence of a perpendicular applied field, according to Sec. 3.2 protocol. Ring 1 is the central ring of this research. Its data appears in the red down-triangles in Fig. 3.1(b). A different offset has been added to each ring to separate the measurements

D.3 Nematic order

Fig. D.3 presents the nematic and superconducting transition temperatures as a function of the Tellurium composition in the FeSeTe sample (reprinted from Mukasa et al. [25]). Panel (b) is focused on a lower temperature range. The nematic transition (T_s) is reflected as a tetragonal to orthorhombic structural transition. The nematic and superconducting transition was measured by resistivity measurements, the blue and red circles in Fig. D.3, respectively. Additionally, the T_s was determined by the splitting of the Bragg peaks in the XRD measurements (the green triangle). The resistivity measurements cannot be used to observe T_s below T_c due to the absence of resistivity. The lowest temperature measured by the XRD measurements is 13.3 K, and there are no measurements close to the 0.5 (Te composition). Nevertheless, it looks like the two transition temperatures converge near 0.5. Maybe there is a composition for which the nematic critical temperature drops below T_c ? Perhaps this happens in our sample (with similar composition), and this is the explanation for the knee.

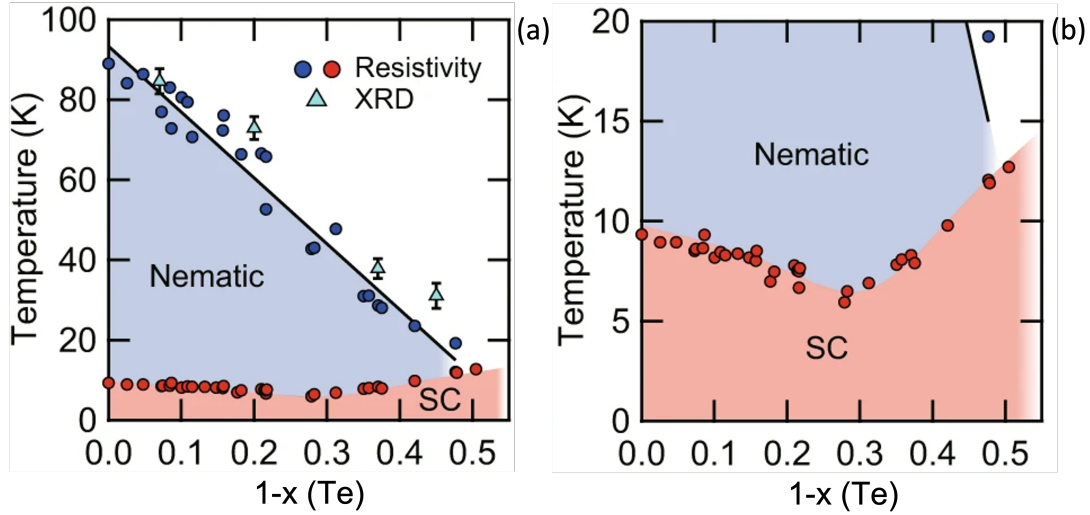


Figure D.3: Transition temperature vs. Te composition. The blue and red circles represent the nematic and superconducting transition temperatures from resistivity measurements. The green triangle represents the nematic temperature determined by the splitting of the Bragg peaks in the XRD measurements. Panel (b) is the same as (a) but focused on a lower temperature range. Reprinted from [25]

D.4 Two critical temperatures?

Peng Zhang et al. [26], suggests the existence of surface superconductivity in FeSeTe, as illustrated in Fig. D.4. This might lead to two different T_c s, one for the bulk SC and one for the surface. The two T_c s can be another reason for the knee.

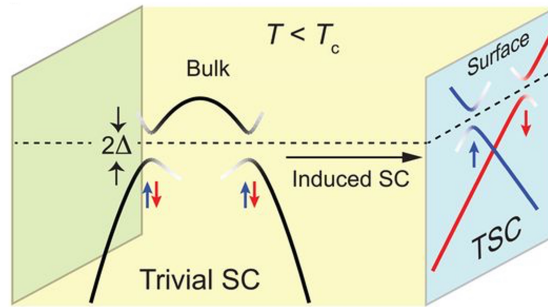


Figure D.4: Superconducting state in the bulk and on the surface. The blue and red arrows illustrate the spin directions. The black curves denote the bulk states, and the blue and red curves to a topological surface states. Reprinted from [26]

Bibliography

- [1] Cao Wang, Linjun Li, Shun Chi, Zengwei Zhu, Zhi Ren, Yuke Li, Yuetao Wang, Xiao Lin, Yongkang Luo, Shuai Jiang, et al. Thorium-doping-induced superconductivity up to 56 k in gd1-xthxfeaso. *EPL (Europhysics Letters)*, 83(6):67006, 2008.
- [2] Andreas Kreisel, Peter J Hirschfeld, and Brian M Andersen. On the remarkable superconductivity of fese and its close cousins. *Symmetry*, 12(9):1402, 2020.
- [3] PK Biswas, G Balakrishnan, DM Paul, CV Tomy, MR Lees, and AD Hillier. Muon-spin-spectroscopy study of the penetration depth of fete 0.5 se 0.5. *Phys. Rev. B*, 81(9):092510, 2010.
- [4] M Bendele, S Weyeneth, R Puzniak, A Maisuradze, E Pomjakushina, K Conder, V Pomjakushin, H Luetkens, S Katrych, A Wisniewski, et al. Anisotropic superconducting properties of single-crystalline fese 0.5 te 0.5. *Phys. Rev. B*, 81(22):224520, 2010.
- [5] Alessandro Serafin, Amalia I Coldea, AY Ganin, MJ Rosseinsky, K Prassides, David Vignolles, and A Carrington. Anisotropic fluctuations and quasiparticle excitations in fese 0.5 te 0.5. *Phys. Rev. B*, 82(10):104514, 2010.
- [6] H Kim, C Martin, RT Gordon, MA Tanatar, J Hu, B Qian, ZQ Mao, Rongwei Hu, Cedomir Petrovic, N Salovich, et al. London penetration depth and superfluid density of single-crystalline fe 1+ y (te 1- x se x) and fe 1+ y (te 1- x s x). *Phys. Rev. B*, 81(18):180503, 2010.
- [7] Hideyuki Takahashi, Yoshinori Imai, Seiki Komiya, Ichiro Tsukada, and Atsutaka Maeda. Anomalous temperature dependence of the superfluid density caused by a dirty-to-clean crossover in superconducting fese 0.4 te 0.6 single crystals. *Phys. Rev. B*, 84(13):132503, 2011.
- [8] Dongfei Wang, Lingyuan Kong, Peng Fan, Hui Chen, Shiyu Zhu, Wenyao Liu, Lu Cao, Yujie Sun, Shixuan Du, John Schneeloch, et al. Evidence for majorana bound states in an iron-based superconductor. *Science*, 362(6412):333–335, 2018.

- [9] Ching-Kai Chiu, T Machida, Yingyi Huang, T Hanaguri, and Fu-Chun Zhang. Scalable majorana vortex modes in iron-based superconductors. *Science advances*, 6(9):eaay0443, 2020.
- [10] Shruti, G Sharma, and S Patnaik. Anisotropy in upper critical field of fete0. 55se0. 45. In *AIP Conference Proceedings*, volume 1665, page 130030. AIP Publishing LLC, 2015.
- [11] Despina Louca, K Horigane, A Llobet, R Arita, S Ji, N Katayama, S Konbu, K Nakamura, T-Y Koo, P Tong, et al. Local atomic structure of superconducting fese 1- x te x. *Physical Review B*, 81(13):134524, 2010.
- [12] Itay Mangel, Itzik Kapon, Nitzan Blau, Katrine Golubkov, Nir Gavish, and Amit Keren. Stiffnessometer: A magnetic-field-free superconducting stiffness meter and its application. *Phys. Rev. B*, 102(2):024502, 2020.
- [13] Nir Gavish, Oded Kenneth, and Amit Keren. Ginzburg–landau model of a stiffnessometer—a superconducting stiffness meter device. *Physica D: Nonlinear Phenomena*, 415:132767, 2021.
- [14] Amit Keren, Nitsan Blau, Nir Gavish, Oded Kenneth, Yachin Ivry, and Mohammad Suleiman. Stiffness and coherence length measurements of ultra-thin superconductors, and implications for layered superconductors. *Superconductor Science and Technology*, 35(7):075013, 2022.
- [15] Marco Beleggia, D Vokoun, and M De Graef. Demagnetization factors for cylindrical shells and related shapes. *Journal of Magnetism and Magnetic Materials*, 321(9):1306–1315, 2009.
- [16] Alarich Weiss. Dj craik (editor): Magnetic oxides, part 1+ 2, jw wiley & sons, london/new york/sydney/toronto 1975, 798 seiten., 1976.
- [17] Jinghui Wang, Song Bao, Yanyan Shangguan, Zhengwei Cai, Yuan Gan, Shichao Li, Kejing Ran, Zhen Ma, Barry L Winn, Andrew D Christianson, et al. Enhanced low-energy magnetic excitations evidencing the cu-induced localization in the fe-based superconductor fe 0.98 te 0.5 se 0.5. *Phys. Rev. B*, 105(24):245129, 2022.
- [18] A Galluzzi, K Buchkov, V Tomov, E Nazarova, A Leo, G Grimaldi, A Nigro, S Pace, and M Polichetti. Evidence of pinning crossover and the role of twin boundaries in the peak effect in fese te iron based superconductor. *Superconductor Science and Technology*, 31(1):015014, 2017.
- [19] Michael Tinkham. *Introduction to superconductivity*. Courier Corporation, 2004.
- [20] Frédéric Hecht. New development in freefem++. *Journal of numerical mathematics*, 20(3-4):251–266, 2012.

- [21] C Varmazis and Myron Strongin. Inductive transition of niobium and tantalum in the 10-mhz range. i. zero-field superconducting penetration depth. *Phys. Rev. B*, 10(5):1885, 1974.
- [22] Pierre-Gilles De Gennes and Philip A Pincus. *Superconductivity of metals and alloys*. CRC Press, 2018.
- [23] D Singh, PK Biswas, AD Hillier, RP Singh, et al. Superconducting properties of the noncentrosymmetric superconductor laptge. *Phys. Rev. B*, 98(21):214505, 2018.
- [24] Tian Shang, Alfred Amon, Deepa Kasinathan, W Xie, Matej Bobnar, Y Chen, A Wang, Ming Shi, Marisa Medarde, HQ Yuan, et al. Enhanced t_c and multiband superconductivity in the fully-gapped rebe22 superconductor. *New Journal of Physics*, 21(7):073034, 2019.
- [25] K Mukasa, K Matsuura, M Qiu, M Saito, Y Sugimura, K Ishida, M Otani, Y Onishi, Y Mizukami, K Hashimoto, et al. High-pressure phase diagrams of fese1-xtex: correlation between suppressed nematicity and enhanced superconductivity. *Nature communications*, 12(1):1–7, 2021.
- [26] Peng Zhang, Koichiro Yaji, Takahiro Hashimoto, Yuichi Ota, Takeshi Kondo, Koza Okazaki, Zhijun Wang, Jinsheng Wen, GD Gu, Hong Ding, et al. Observation of topological superconductivity on the surface of an iron-based superconductor. *Science*, 360(6385):182–186, 2018.

סלניום או טלור הממוקמים במבנה טטראדר.

בעבודה זו מוצגות מגוון מדידות אשר נעשו על מנת לאפיין את תכונותיו העל-מוליכות והמגנטיות של הגביש, המרכזיות ביניהם הינם: (1) מדידת קשיחות. מדידת מומנט כתלות בזרם בסליל הערעור בטמפרטורות שונות מתחת ל- T_c . מדידה זו ממחישה את הקשר של משוואת לונדון ומשמשת למציאת קשיחות העל-מוליך ואורך הקוהרנטית מתוך הזרם הקריטי; (2) מדידת טמפרטורה קריטית. מדידות מומנט כתלות בטמפרטורה בהשפעת זרמים בסליל הערעור או בהשפעת שדה מגנטי חיצוני ואחיד. מדידות אלו משמשות לגלות את הטמפרטורה הקריטית ואת הסוספטביליות המגנטית; (3) לולאת היסטורסיס. מדידת מומנט כתלות בשדה מעל הטמפרטורה הקריטית לגילוי פרומגנטיות; (4) מדידת שדות קריטיים. מדידת מומנט כתלות בשדה המגנטי בטמפרטורות שונות מתחת ל- T_c . משמש למציאת התלות בטמפרטורה של השדה הקריטי הראשון והשני. בנוסף, במהלך הניסוי התברר כי הזרמת זרם בסליל הערעור שעשוי מנחושת יוצר גרדינט טמפרטורות בין הטבעת לטרמוסטט במקרה. לשם כיוול הטמפרטורה נדרשנו לחשוב על ניסוי חדש המאפשר לזהות את הטמפרטורה האמיתית של הטבעת.

תקציר

קשיחות העל-מוליך ρ_s מביעה את היחס שבין הפוטנציאל הוקטורי A וצפיפות זרם העל-מוליך j בתוך על-מוליך לפי משוואת לונדון $j = -\rho_s A$. אורך הקוהרנטיות הוא השני מבין שני פרמטרי האורך של על-מוליכות בתורה של גינזבורג-לנדאו. גודל זה מאפיין את המרחק הקצר ביותר בו פרמטר הסדר $\Psi(r)$ יכול להשתנות מבלי לגרום לעלייה מיותרת באנרגיה. זהו גודל חשוב בהרבה תחומי מחקר של על-מוליכות ולכן יש לנו מוטיבציה למדוד אותו. בדרך כלל קשיחות העל-מוליך ואורך הקוהרנטיות נמדדים על ידי הפעלת שדות מגנטיים חיצוניים ומדידת עומק החדירה שלהם לתוך החומר λ והשדה הקריטי השני H_{c2} . למרות זאת, בחומרים מגנטיים כגון חלק ממשפחת העל-מוליכים מבוססי ברזל ותרכובת ברזל-סלניום-טלור (FeSeTe) בפרט. בעיה זו יכולה להוביל לתוצאות שגויות מאחר והשדה המגנטי מתערבב עם השדה המגנטי שהחומר יוצר. על מנת להתגבר על בעיה זו אנו משתמשים בשיטה חדשה למדידת קשיחות העל-מוליך ואורך הקוהרנטיות הנקראת "קשיחות" (Stiffnessometer) אשר פותחה בקבוצת המחקר שלנו. בשיטה זו חותכים את הגביש לצורת טבעת ומקבעים אותה במרכזו של סליל ארוך מאוד הנקרא סליל עירור. הזרמת זרם בסליל העירור יוצרת שדה מגנטי בחלקו הפנימי של הסליל בלבד, לאומת זאת, נוצר וקטור פוטנציאל A חסר רוטור וללא שדה מגנטי בטבעת העל-מוליכה. לפי משוואת לונדון מתעוררים בטבעת זרמי התמד על-מוליכים אשר מקיפים את הטבעת. צפיפות הזרם בטבעת j נמדדת דרך המומנט המגנטי של העל-מוליך M באמצעות מגנטומטר סקויד (התקן התאבכות קוונטית על-מוליך SQUID), ומכיוון שעוצמת הזרם בסליל הערעור ידועה לנו, ניתן לחשב את וקטור הפוטנציאל המופעל ולחשב את הקשיחות מתוך משוואת לונדון. על-ידי הגברת הזרם שעובר בסליל העירור ניתן לסחוף את הפוטנציאל הוקטורי המגנטי עד שהקשר הלינארי בין j ל- A נשבר. מתוך פתרון של משוואות גינזבורג-לנדאו בתחומים המתאימים ניתן לקשר את הצפיפות הזרם הקריטית לאורך הקוהרנטיות. שיטה זו מדויקת במיוחד בקרבת הטמפרטורה הקריטית. היא מאפשרת לחקור על-מוליכים ללא שימוש במגעים או נוכחות של שדה מגנטי בדגם, באופן זה אנו נמנעים מסיבוכים של גורם דימגנטיזציה, ומקיומם של מערבולות זרם (Vortices). בעבודה זו מתבצעת השוואה בין תוצאותינו לציפיות תיאורטיות ולטכניקות מדידה שונות.

על מוליכות בטמפרטורות גבוהות התגלתה בשנות השמונים במשפחה של חומרים שהמשותף להם הוא מישורים אטומיים עשויים נחושת וחמצן. בשנת 2008 התגלתה משפחה נוספת של על-מוליכים בעלי טמפרטורה קריטית גבוהה שהמשותף להם הוא מישורים אטומיים של ברזל. באותה השנה התגלתה לראשונה על-מוליכות בגבישי ברזל-סלניום עם טמפרטורה קריטית של 8 מעלות קלווין בלחץ אטמוספרי. החלפת חלק מאטומי הסלניום באטומי טלור הוביל לעליה של הטמפרטורה קריטית עד לטמפרטורה מקסימאלית של 15 מעלות קלווין אשר התקבלה עבור $x = 0.45$ $(y \simeq 0)$ בנוסחה $\text{Fe}_{1+y}\text{Se}_x\text{Te}_{1-x}$. מבנה הגביש שלו מכיל משכבה מישורית של אטומי ברזל המחוברים על ידי אטומי

המחקר בוצע בהנחייתו של פרופסור עמית קרן בפקולטה לפיזיקה.

הכרת תודה מסורה לטכניון על מימון מחקר זה.

מדידת קשיחות ואורך הקוהרנטיות של על-מוליכים מגנטיים בשדה מגנטי אפס, ויישום על תרכובת ברזל-סלניום-טלור

חיבור על מחקר

לשם מילוי חלקי של הדרישות לקבלת התואר
מגיסטר למדעים בפיזיקה

אמוץ פרי

הוגש לסנט הטכניון – מכון טכנולוגי לישראל
אלול התשפ"ב חיפה אוגוסט 2022

**מדידת קשיחות ואורך הקוהרנטיות של
על-מוליכים מגנטיים בשדה מגנטי אפס,
ויישום על תרכובת ברזל-סלניום-טלור**

אמוץ פרי